Fiber-based polarization-sensitive Fourier domain optical coherence tomography using B-scan-oriented polarization modulation method

Masahiro Yamanari, Shuichi Makita, Violeta Dimitrova Madjarova, Toyohiko Yatagai, and Yoshiaki Yasuno

Computational Optics Group, Institute of Applied Physics, University of Tsukuba, 1-1-1 Tennodai, Tsukuba, Ibaraki, Japan

yamanari@optlab2.bk.tsukuba.ac.jp

http://optics.bk.tsukuba.ac.jp/COG/

Abstract: Fiber-based high-speed polarization-sensitive Fourier domain optical coherence tomography (PS-FD-OCT) is developed at 840 nm wavelengh using polarization modulation method. The incident state of polarization is modulated along B-scan. The spectrometer has a polarizing beamsplitter and two line-CCD cameras operated at a line rate of 27.7 kHz. From the 0th and 1st orders of the spatial frequencies along the B-scanning, a depth-resolved Jones matrix can be derived. Since continuous polarization modulation along B-scan causes fringe washout, equivalent discrete polarization modulation is applied to biological measurements. For the demonstration, an *in vitro* chicken breast muscle, an *in vivo* finger pad, and an *in vivo* caries lesion of a human tooth are measured. Three dimensional phase retardation images show the potentials for applying the system to biological and medical studies.

OCIS codes: (170.4500) Optical coherence tomography; (120.2130) Ellipsometry and polarimetry; (170.3880) Medical and biological imaging; (260.1440) Birefringence; (110.4500) Optical coherence tomography.

References and links

1. D. Huang, E. A. Swanson, C. P. Lin, J. S. Schuman, W. G. Stinson, W. Chang, M. R. Hee, T. Flotte, K. Gregory, C. A. Puliafito, and J. G. Fujimoto, "Optical coherence tomography," Science **254**, 1178–1181 (1991).
2. M. R. Hee, D. Huang, E. A. Swanson, and J. G. Fujimoto, "Polarization-sensitive low-coherence reflectometer for birefringence characterization and ranging," J. Opt. Soc. Am. B **9**, 903–908 (1992).
3. J. F. de Boer, T. E. Milner, M. J. C. van Gemert, and J. S. Nelson, "Two-dimensional birefringence imaging in biological tissue by polarization-sensitive optical coherence tomography," Opt. Lett. **22**, 934–936 (1997).
4. J. F. de Boer, S. M. Srinivas, A. Malekafzali, Z. Chen, and J. S. Nelson, "Imaging thermally damaged tissue by polarization sensitive optical coherence tomography," Opt. Express **3**, 212–218 (1998).
5. K. Schoenenberger, J. B. W. Colston, D. J. Maitland, L. B. Da Silva, and M. J. Everett, "Mapping of birefringence and thermal damage in tissue by use of polarization-sensitive optical coherence tomography," Appl. Opt., **37**, 6026–6036 (1998).
6. B. H. Park, C. Saxer, S. M. Srinivas, J. S. Nelson, and J. F. de Boer, "In vivo burn depth determination by high-speed fiber-based polarization sensitive optical coherence tomography," J. Biomed. Opt. **6**, 474–479 (2001).
7. S. Jiao and L. V. Wang, "Jones-matrix imaging of biological tissues with quadruple-channel optical coherence tomography," J. Biomed. Opt. **7**, 350–358 (2002).

#70056 - $15.00 USD Received 18 April 2006; revised 28 June 2006; accepted 29 June 2006

8. S. Jiao, W. Yu, G. Stoica, and L. V. Wang, "Contrast mechanisms in polarization-sensitive Mueller-matrix optical coherence tomography and application in burn imaging," Appl. Opt. **42**, 5191–5197 (2003).
9. M. C. Pierce, J. Strasswimmer, B. H. Park, B. Cense, and J. F. de Boer, "Advances in optical coherence tomography imaging for dermatology," J. Invest. Dermatol. **123**, 458–463 (2004).
10. S. M. Srinivas, J. F. de Boer, H. Park, K. Keikhanzadeh, H. L. Huang, J. Zhang, W. Q. Jung, Z. Chen, and J. S. Nelson, "Determination of burn depth by polarization-sensitive optical coherence tomography," J. Biomed. Opt. **9**, 207–212 (2004).
11. M. Pircher, E. Goetzinger, R. Leitgeb, and C. K. Hitzenberger, "Transversal phase resolved polarization sensitive optical coherence tomography," Phys. Med. Biol. **49**, 1257-1263 (2004).
12. E. Götzinger, M. Pircher, M. Sticker, A. F. Fercher, and C. K. Hitzenberger, "Measurement and imaging of birefringent properties of the human cornea with phase-resolved, polarization-sensitive optical coherence tomography," J. Biomed. Opt. **9**, 94–102 (2004).
13. M. G. Ducros, J. F. de Boer, H. Huang, L. C. Chao, Z. Chen, J. S. Nelson, T. E. Milner, and I. H. G. Rylander, III, "Polarization sensitive optical coherence tomography of the rabbit eye," IEEE J. Sel. Top. Quantum Electron. **5**, 1159–1167 (1999).
14. M. G. Ducros, J. D. Marsack, H. G. Rylander III, S. L. Thomsen, and T. E. Milner, "Primate retina imaging with polarization-sensitive optical coherence tomography," J. Opt. Soc. Am. A **18**, 2945–2956 (2001).
15. B. Cense, T. C. Chen, B. H. Park, M. C. Pierce, and J. F. de Boer, "Thickness and birefringence of healthy retinal nerve fiber layer tissue measured with polarization-sensitive optical coherence tomography," Invest. Ophthalmol. Vis. Sci. **45**, 2606–2612 (2004).
16. B. Cense, T. C. Chen, B. H. Park, M. C. Pierce, and J. F. de Boer, "*In vivo* birefringence and thickness measurements of the human retinal nerve fiber layer using polarization-sensitive optical coherence tomography," J. Biomed. Opt. **9**, 121–125 (2004).
17. E. Götzinger, M. Pircher, and C. K. Hitzenberger, "High speed spectral domain polarization sensitive optical coherence tomography of the human retina," Opt. Express **13**, 10,217–10,229 (2005).
18. N. J. Kemp, J. Park, H. N. Zaatari, H. G. Rylander, and T. E. Milner, "High-sensitivity determination of birefringence in turbid media with enhanced polarization-sensitive optical coherence tomography," J. Opt. Soc. Am. A **22**, 552–560 (2005).
19. X. Wang, T. E. Milner, J. F. de Boer, Y. Zhang, D. H. Pashley, and J. S. Nelson, "Characterization of dentin and enamel by use of optical coherence tomography," Appl. Opt. **38**, 2092–2096 (1999).
20. A. Baumgartner, S. Dichtl, C. K. Hitzenberger, H. Sattmann, B. Robl, A. Moritz, A. F. Fercher, and W. Sperr, "Polarization-sensitive optical coherence tomography of dental structures," Caries Res. **34**, 59–69 (2000).
21. D. Fried, J. Xie, S. Shafi, J. D. B. Featherstone, T. M. Breunig, and C. Le, "Imaging caries lesions and lesion progression with polarization sensitive optical coherence tomography," J. Biomed. Opt. **7**, 618–627 (2002).
22. Y. Chen, L. Otis, D. Piao, and Q. Zhu, "Characterization of dentin, enamel, and carious lesions by a polarization-sensitive optical coherence tomography system," Appl. Opt. **44**, 2041–2048 (2005).
23. R. S. Jones, C. L. Darling, J. D. B. Featherstone, and D. Fried, "Remineralization of *in vitro* dental caries assessed with polarization-sensitive optical coherence tomography," J. Biomed. Opt **11**, 014016 (2006).
24. M. C. Pierce, M. Shishkov, B. H. Park, N. A. Nassif, B. E. Bouma, G. J. Tearney, and J. F. de Boer, "Effects of sample arm motion in endoscopic polarization-sensitive optical coherence tomography," Opt. Express **13**, 5739–5749 (2005).
25. J. J. Pasquesi, S. C. Schlachter, M. D. Boppart, E. Chaney, S. J. Kaufman, and S. A. Boppart, "*In vivo* detection of exercise-induced ultrastructural changes in genetically-altered murine skeletal muscle using polarization-sensitive optical coherence tomography," Opt. Express **14**, 1547–1556 (2006).
26. C. K. Hitzenberger, E. Götzinger, M. Sticker, M. Pircher, and A. F. Fercher, "Measurement and imaging of birefringence and optic axis orientation by phase resolved polarization sensitive optical coherence tomography," Opt. Express **9**, 780–790 (2001).
27. R. Leitgeb, C. K. Hitzenberger, and A. F. Fercher, "Performance of fourier domain vs. time domain optical coherence tomography," Opt. Express **11**, 889–894 (2003).
28. J. F. de Boer, B. Cense, B. H. Park, M. C. Pierce, G. J. Tearney, and B. E. Bouma, "Improved signal-to-noise ratio in spectral-domain compared with time-domain optical coherence tomography," Opt. Lett. **28**, 2067–2069 (2003).
29. J. F. de Boer, T. E. Milner, and J. S. Nelson, "Determination of the depth-resolved Stokes parameters of light backscattered from turbid media by use of polarization-sensitive optical coherence tomography," Opt. Lett. **24**, 300–302 (1999).
30. C. E. Saxer, J. F. de Boer, B. H. Park, Y. Zhao, Z. Chen, and J. S. Nelson, "High-speed fiber-based polarzation-sensitive optical coherence tomography of *in vivo* human skin," Opt. Lett. **25**, 1355–1357 (2000).
31. J. Zhang, W. Jung, J. S. Nelson, and Z. Chen, "Full range polarization-sensitive Fourier domain optical coherence tomography," Opt. Express **12**, 6033–6039 (2004).
32. B. Cense, T. C. Chen, M. Mujat, C. Joo, T. Akkin, B. H. Park, M. C. Pierce, A. Yun, B. E. Bouma, G. J. Tearney, and J. F. de Boer, "Spectral-domain polarization-sensitive optical coherence tomography at 850 nm," Proc. of SPIE **5690**, 159–162 (2005).

#70056 - $15.00 USD Received 18 April 2006; revised 28 June 2006; accepted 29 June 2006

33. G. Yao and L. V. Wang, "Two-dimensional depth-resolved Mueller matrix characterization of biological tissue by optical coherence tomography," Opt. Lett. **24**, 537–539 (1999).
34. Y. Yasuno, S. Makita, Y. Sutoh, M. Itoh, and T. Yatagai, "Birefringence imaging of human skin by polarization-sensitive spectral interferometric optical coherence tomography," Opt. Lett. **27**, 1803–1805 (2002).
35. S. H. Yun, G. J. Tearney, J. F. de Boer, and B. E. Bouma, "Motion artifacts in optical coherence tomography with frequency-domain ranging," Opt. Express **12**, 2977–2998 (2004).
36. S. Jiao, G. Yao, and L. V. Wang, "Depth-resolved two-dimensional Stokes vectors of backscattered light and Mueller matrices of biological tissue measured with optical coherence tomography," Appl. Opt. **39**, 6318–6324 (2000).
37. J. F. de Boer and T. E. Milner, "Review of polarization sensitive optical coherence tomography and Stokes vector determination," J. Biomed. Opt. **7**, 359–371 (2002).
38. S. Jiao and L. V. Wang, "Two-dimensional depth-resolved Mueller matrix of biological tissue measured with double-beam polarization-sensitive optical coherence tomography," Opt. Lett. **27**, 101–103 (2002).
39. S. Jiao, G. S. W. Yu, and L. V. Wang, "Optical-fiber-based Mueller optical coherence tomography," Opt. Lett. **28**, 1206–1208 (2003).
40. B. H. Park, M. C. Pierce, B. Cense, and J. F. de Boer, "Jones matrix analysis for a polarization-sensitive optical coherence tomography system using fiber-optic components," Opt. Lett. **29**, 2512–2514 (2004).
41. B. H. Park, M. C. Pierce, B. Cense, S. H. Yun, M. Mujat, G. J. Tearney, B. E. Bouma, and J. F. de Boer, "Real-time fiber-based multi-functional spectral-domain optical coherence tomography at 1.3 μm,," Opt. Express **13**, 3931–3944 (2005).
42. S. Guo, J. Zhang, L. Wang, J. S. Nelson, and Z. Chen, "Depth-resolved birefringence and differential optical axis orientation measurements with fiber-based polarization-sensitive optical coherence tomography," Opt. Lett. **29**, 2025–2027 (2004).
43. M. Todorović, S. Jiao, L. V. Wang, and G. Stoica, "Determination of local polarization properties of biological samples in the presence of diattenuation by use of Mueller optical coherence tomography," Opt. Lett. **29**, 2402–2404 (2004).
44. S. Makita, Y. Yasuno, T. Endo, M. Itoh, and T. Yatagai, "Polarization contrast imaging of biological tissues by polarization-sensitive Fourier-domain optical coherence tomography," Appl. Opt. **45**, 1142–1147 (2005).
45. S. Jiao, M. Todorović, G. Stoica, and L. V. Wang, "Fiber-based polarization-sensitive Mueller matrix optical coherence tomography with continuous source polarization modulation," Appl. Opt. **44**, 5463–5467 (2005).
46. S. N. Jasperson, and S. E. Schnatterly, "An improved method for high reflectivity ellipsometry based on a new polarization modulation technique," Rev. Sci. Instrum. **40**, 761–767 (1969).
47. Y. Yasuno, S. Makita, T. Endo, M. Itoh, T. Yatagai, M. Takahashi, C. Katada, and M. Mutoh, "Polarization-sensitive complex Fourier domain optical coherence tomography for Jones matrix imaging of biological samples," Appl. Phys. Lett. **85**, 3023–3025 (2004).
48. B. R. White, M. C. Pierce, N. Nassif, B. Cense, B. H. Park, G. J. Tearney, B. E. Bouma, T. C. Chen, and J. F. de Boer, "*In vivo* dynamic human retinal blood flow imaging using ultra-high-speed spectral domain optical Doppler tomography," Opt. Express **11**, 3490–3497 (2003).
49. M. Wojtkowski, V. J. Srinivasan, T. H. Ko, J. G. Fujimoto, A. Kowalczyk, and J. S. Duker, "Ultrahigh-resolution, high-speed, Fourier domain optical coherence tomography and methods for dispersion compensation," Opt. Express **12**, 2404–2422 (2004).
50. B. H. Park, M. C. Pierce, B. Cense, and J. F. de Boer, "Optic axis determination accuracy for fiber-based polarization-sensitive optical coherence tomography," Opt. Lett. **30**, 2587–2589 (2005).
51. M. C. Pierce, J. Strasswimmer, B. H. Park, B. Cense, and J. F. de Boer, "Birefringence measurements in human skin using polarization-sensitive optical coherence tomography," J. Biomed. Opt. **9**, 287–291 (2004).
52. M. Pircher, E. Goetzinger, R. Leitgeb, and C. K. Hitzenberger, "Three dimensional polarization sensitive OCT of human skin *in vivo*," Opt. Express **12**, 3236–3244 (2004).

1. Introduction

Optical coherence tomography (OCT) has been developed to measure depth-resolved images of various biological tissues [1]. In addition to the intensity image of biological sample, polarization-sensitive optical coherence tomography (PS-OCT) also visualizes its birefringence [2, 3]. It is well known that some biological tissues have a microscopic fibrous structure and the resultant form birefringence. The PS-OCT detects the depth-resolved birefringence including the form birefringence of a biological tissue. Several papers have reported the applications of the PS-OCT, for example, its applications to burn lesion of skin [4, 5, 6, 7, 8, 9, 10], cornea [11, 12], retina [13, 14, 15, 16, 17, 18], dentistry [19, 20, 21, 22, 23], and endoscopy [24]. Recently, Pasquesi et al. reported that the PS-OCT can detect ultrastructural changes in a muscle

#70056 - $15.00 USD Received 18 April 2006; revised 28 June 2006; accepted 29 June 2006

using the changes in the form birefringence related to dystrophy [25].

Several methods have been developed to detect the birefringence with the PS-OCT. Table 1 summarizes the typical approaches used to obtain the primary PS-OCT images. When the optical system is constructed in the free space, the orientation and the phase retardation of the birefringence of the sample can be directly obtained from two orthogonally polarized phase-resolved signals of the time-domain OCT (TD-OCT) [26]. This method was applied to Fourier-domain OCT (FD-OCT) [17], because the FD-OCT enabled faster measurement and higher signal-to-noise ratio as compared to the TD-OCT [27, 28]. Another method using the Stokes vector [29] can be used to visualize the changes in the polarization on the Poincaré sphere [6]. Fiber-based PS-OCT was first demonstrated by Saxer et al. with the Stokes vector method [30]. This method has also been demonstrated with swept-source OCT [31] and spectral-domain OCT [32]. Mueller matrix, which can describe the complete polarization property of a sample, was first measured with OCT by Yao et al. [33]. Yasuno et al. first demonstrated PS-FD-OCT using this Mueller matrix method [34].

When the sample is unstable during *in vivo* measurement, fringe washout in the phase-sensitive measurement [35] occures instead of the depolarization in the intensity-based measurement [36, 37]. We can apply Jones matrix to show the polarization property of the sample using the phase-resolved signals [38]. Based on the Jones matrix analysis, a compensation method of the fiber-induced birefringence was developed by Jiao et al. for fibers in the reference and sample arms [39]. Subsequently, Park et al. developed a more general compensating algorithm in order to use other convenient fiber components in the TD-OCT [40], and applied the algorithm to the FD-OCT [41].

In general, the PS-OCT detects cumulative round-trip phase retardation. Local birefringence was calculated based on the Stokes vector method [42] and the Jones matrix method [43, 44]. Kemp et al. developed a polarimetric speckle reduction method to show the overall change in the Stokes vector on the Poincaré sphere [18].

Recently, Jiao et al. [45] developed the novel scheme of continuous polarization modulation that was a conventional technique in the field of ellipsometry [46]. In their TD-OCT system, the incident polarization was modulated along the axial scan.

Table 1. Typical approaches to obtain PS-OCT image. A: circularly polarized incident light, B: Stokes vector, C: Mueller matrix, D: Jones matrix with two incident polarizations, E: Jones matrix with polarization modulation method.

	Time-domain		Fourier-domain	
	Free space	Fiber-based	Free space	Fiber-based
A	Hee et al. [2] de Boer et al. [3] Hitzenberger et al. [26]		Götzinger et al. [17]	
B	de Boer et al. [29]	Saxer et al. [30]		Zhang et al. [31] Cense et al. [32]
C	Yao et al. [33]		Yasuno et al. [34]	
D	Jiao et al. [38]	Jiao et al. [39] Park et al. [40]	Yasuno et al. [47]	Park et al. [41]
E		Jiao et al. [45]		◇

In this paper, the algorithm of the polarization modulation method [43, 45] is applied to the FD-OCT, indicated by ◇ in Table 1. Fiber components and a polarization-sensitive spectrometer

#70056 - $15.00 USD Received 18 April 2006; revised 28 June 2006; accepted 29 June 2006

are used for the optical setup. The incident polarized light is modulated along a lateral B-scan instead of an axial A-scan. The Jones matrix of the sample is obtained from the spatial frequencies of the B-scan. Fiber-induced birefringence is compensated by using the algorithm developed by Park et al. [40]

2. The optical system and the synchronization system

2.1. Overview

The diagram of our system is shown in Fig. 1. The light source is a superluminescent diode (SLD-37-HP, Superlum, Russia) with a central wavelength of 840 nm, bandwidth of 50 nm, and axial resolution of 8.3 μm in air. After the polarization is vertically aligned by a linear polarizer (LP), an EO modulator (4104, New Focus, CA, USA) with a fast axis of 45° modulates the incident polarization. The modulated light is coupled into a 30/70 fiber coupler. 30% of the incident light is delivered into the sample arm, and 70% is delivered into the reference arm. This splitting ratio was selected for the future application of retinal measurement to conform to a safety standard of the illumination power. An LP is inserted in the reference arm to obtain constant amplitude and constant relative phase between the two orthogonal polarizations at the spectrometer independent of the incident state of the polarization. This configuration was achieved by an iterative alignment of the polarization controller and LP in the reference arm. In the sample arm, the 1.5 mm diameter beam focused by a 50 mm focal length lens is scanned by the two-axis galvanoscanner mirror. The probing power is 700 μW. The theoretical transversal resolution and focal depth are 36 μm and 2.4 mm, respectively. The backscattered light from the sample goes through the fiber coupler again, and is detected by the spectrometer. In the spectrometer, the interfered beam is collimated with a 120 mm focal length lens, dispersed by a polarization-insensitive volume phase holographic grating of 1200 lines/mm (Wasatch Photonics, UT, USA), spatially Fourier transformed by a 250 mm focal length lens, divided into horizontally and vertically polarized components by a polarizing beamsplitter, and detected by two line-CCD cameras of 2048 pixels and 14 μm pixel size (AVIIVA M2 CL 2014, Atmel, CA, USA). A line trigger for both cameras (27.7 kHz) is generated by a DAQ board and synchronized with the galvanoscanner mirror in the sample arm and the EO modulator. The waveform driving the galvanoscanner mirror is a sawtooth wave, and that driving the EO modulator is a sinusoidal wave or a three-step function. The further details are described in Sec. 3. The data from both cameras are acquired by a framegrabber (PCIe-1430, National Instruments, TX, USA). The sensitivity of the system is 100.7 dB, which is obtained by adding the horizontal and vertical channels. The phase stability is 3.24 degrees at the signal-to-noise ratio of 27.6 dB, which is reasonably stable for this signal-to-noise ratio [41].

2.2. Calibration of the polarization-sensitive spectrometer

Since two line-CCD cameras are used to detect both phase-resolved horizontally and vertically polarized signals, these two cameras must construct two identical spectrometers. Park et al. explained the method of the calibration briefly [41]. Götzinger et al. derived the equations of the effect of the misalignment of the spectrometer [17]. Since the pixel size of our line-CCD cameras is smaller than that of previously reported 1.3μm system [41], finer calibration is required. In this section, we describe our detailed method of the calibration. In order to calibrate these two spectrometers, the EO modulation is stopped. The reference light is blocked, and a slide glass and mirror are placed in the sample arm. This configuration ensures that the positions of the peak are the same for the horizontal and vertical channels. If both the reference and sample arms are used for the calibration in the fiber-based system, random birefringence of the reference and the sample arms causes a random phase difference between the horizontally and vertically polarized components of the OCT signals detected by these two spectrometers. Since

#70056 - $15.00 USD Received 18 April 2006; revised 28 June 2006; accepted 29 June 2006

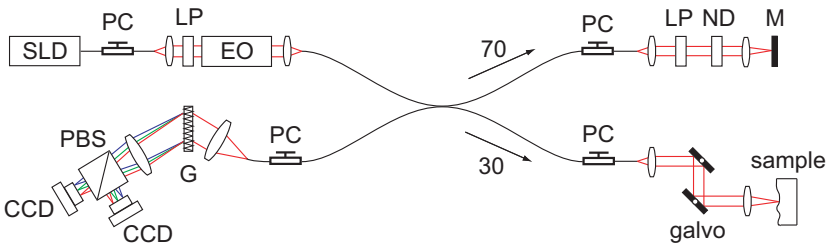

Fig. 1. Diagram of the PS-FD-OCT system. The notations imply the following: SLD: superluminescent diode, PC: polarization controller, ND: neutral density filter, LP: linear polarizer, EO: electro-optic modulator, M: mirror, G: grating, PBS: polarizing beamsplitter, CCD: line-CCD camera.

the position of the fiber can easily change during the calibration, it is efficient to use only one arm of the interferometer. The OCT signals from the back surface of the glass and mirror are obtained for these two spectrometers. The phase difference at the peak of the OCT signals is monitored. This phase difference should be zero for all axial depths. In addition, the signals are windowed and inverse Fourier transformed to obtain the complex spectrum for the two spectrometers. This spectral phase difference is also monitored because it should be zero for all frequencies. By monitoring these values, the physical positions of the two cameras are aligned to minimize the phase difference. Since fine calibration is needed, both the cameras are mounted on the translation stages including the $XYZ\theta\alpha$ axes, where XYZ are the axes of Cartesian coordinates (X and Y are parallel and perpendicular to the line-CCD, respectively, and Z is the height); θ, a tilt of the line-CCD on the XY plane; and α, a tilt on the XZ plane. The optical table on which the spectrometer is built should be rigid, and air fluctuation should be avoided. After the physical calibration, the remaining difference is numerically compensated by adjusting the 0th and 1st order coefficients of the wavelength-frequency rescaling parameters. To verify the calibration, we measured OCT signals between the slide glass and mirror at different axial depth. Figure 2 represents the phase difference between the OCT signals from two channels with respect to the axial depth. The phase difference is within ± 4 deg for all axial depths.

3. Theory

In this section, we describe our algorithm and the calibration method used to obtain a Jones matrix OCT image.

3.1. The Jones matrix imaging method using polarization modulation method along lateral B-scan

We denote the horizontally polarized component of the intensity of the interfered light at the spectrometer as I_h. It can be expressed as

$$I_h(x,\omega) = |H_{ref}(x,\omega)|^2 + |H_{sam}(x,\omega)|^2 + H_{ref}(x,\omega)H^*_{sam}(x,\omega) + c.c., \tag{1}$$

where $H_{ref}(x,\omega)$ and $H_{sam}(x,\omega)$ are the horizontally polarized temporal spectral components of the reference beam and sample beam, respectively, and c.c. denotes the complex conjugate of the third term on the right-hand-side of Eq. (1). The superscript * denotes the complex conjugate, and ω is the optical frequency. The third term in Eq. (1) is extracted and inverse Fourier transformed to obtain the complex OCT signal,

$$\tilde{I}_h(x,z) = \mathscr{F}^{-1}_{z\omega}[H_{ref}(x,\omega)H^*_{sam}(x,\omega)], \tag{2}$$

#70056 - $15.00 USD Received 18 April 2006; revised 28 June 2006; accepted 29 June 2006

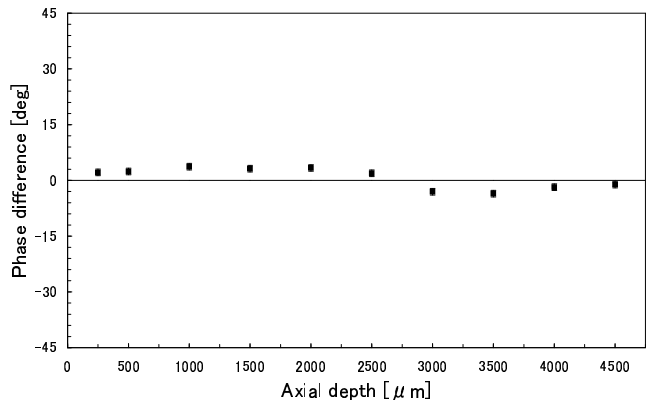

Fig. 2. Depth-dependent phase difference of the OCT signals between horizontal and vertical channels. The interference signal is generated by the back surface of the slide glass and the mirror.

where the axial depth z is the Fourier conjugate of ω, and $\mathscr{F}^{-1}_{z\omega}[\cdot]$ is the inverse Fourier transform about z. Before calculating Eq. (2), the measured power spectrum is rescaled with zero padding and linear interpolation, and the dispersion between the reference arm and sample arm is compensated numerically [49]. In the same manner, the vertical interference term $\tilde{I}_v(x,z)$ is extracted from the vertically polarized component of the interfered light $I_v(x,\omega)$.

When the fast axis of the EO modulator is oriented at $\pi/4$, the Jones matrix of the EO modulator can be expressed as

$$\begin{pmatrix} \cos\frac{\varphi}{2} & i\sin\frac{\varphi}{2} \\ i\sin\frac{\varphi}{2} & \cos\frac{\varphi}{2} \end{pmatrix}, \tag{3}$$

where φ is the phase retardation and modulated as $\varphi(x) = A_0\sin(\omega_m x)$. ω_m is the driving frequency of the EO modulator, and x is the lateral position. As described in Sec. 3.3, discrete polarization modulation can also be used for the phase modulation of the EO modulator.

The Jones vector of the sample beam at the detector can be written as

$$\begin{pmatrix} H_{sam} \\ V_{sam} \end{pmatrix} = \mathrm{J}_{all}\begin{pmatrix} H_i \\ V_i \end{pmatrix}, \tag{4}$$

where J_{all} is the overall round-trip Jones matrix including the birefringence of both the fiber and sample,

$$\mathrm{J}_{all} = \begin{pmatrix} \mathrm{J}(1,1) & \mathrm{J}(1,2) \\ \mathrm{J}(2,1) & \mathrm{J}(2,2) \end{pmatrix}, \tag{5}$$

and $(H_i, V_i)^T$ is the Jones vector just after the EO modulator before the fiber coupler. When the incident beam to the EO modulator is vertically polarized,

$$\begin{pmatrix} H_i \\ V_i \end{pmatrix} = \begin{pmatrix} i\sin\frac{\varphi}{2} \\ \cos\frac{\varphi}{2} \end{pmatrix}. \tag{6}$$

The Jones vector $(H_{sam}, V_{sam})^T$ can be expressed as

$$\begin{pmatrix} H_{sam} \\ V_{sam} \end{pmatrix} = \begin{pmatrix} \mathrm{J}(1,2)\cos\frac{\varphi}{2} + i\mathrm{J}(1,1)\sin\frac{\varphi}{2} \\ \mathrm{J}(2,2)\cos\frac{\varphi}{2} + i\mathrm{J}(2,1)\sin\frac{\varphi}{2} \end{pmatrix}. \tag{7}$$

#70056 - $15.00 USD Received 18 April 2006; revised 28 June 2006; accepted 29 June 2006

The Jones vector of the reference beam at the spectrometer is calibrated to be

$$\mathrm{E}_{ref} = \begin{pmatrix} H_{ref} \\ V_{ref} \end{pmatrix} = \begin{pmatrix} H_r \\ V_r \end{pmatrix} e^{-i\frac{\varphi}{2}}, \tag{8}$$

where H_r and V_r are constants independent of the state of the EO modulator. The reference beam intensity at the CCD cameras should be flat and independent of the phase retardation of the EO modulator.

In our algorithm, Eq. (2) is Fourier transformed along x as

$$\mathscr{F}_{xu}[\tilde{I}_h(x)] = \mathscr{F}_{xu}[\mathscr{F}_{z\omega}^{-1}[H_{ref}(x,\omega)H_{sam}^*(x,\omega)]] \tag{9}$$

where $\mathscr{F}_{xu}[\cdot]$ is Fourier transform operator along x, and u is the Fourier conjugate of x. Equation (9) can be rearranged as

$$\begin{aligned}\mathscr{F}_{xu}[\tilde{I}_h(x)] =& H_r\mathscr{F}_{xu}[\mathrm{J}^*(1,2)\cos\frac{\varphi}{2}e^{-i\frac{\varphi}{2}} - i\mathrm{J}^*(1,1)\sin\frac{\varphi}{2}e^{-i\frac{\varphi}{2}}] \\ =& \frac{H_r}{2}\{\mathscr{F}_{xu}[\mathrm{J}^*(1,2)-\mathrm{J}^*(1,1)] + \mathscr{F}_{xu}[\mathrm{J}^*(1,2)+\mathrm{J}^*(1,1)] * \mathscr{F}_{xu}[e^{-i\varphi}]\},\end{aligned} \tag{10}$$

where $*$ denotes a convolution operator. Here, we omitted the argument z of these functions for simplicity. $e^{i\varphi}$ can be decomposed using the following relations:

$$\sin[\varphi(x)] = \sum_{l=0}^{\infty} 2J_{2l+1}(A_0)\sin[(2l+1)\omega_m x], \tag{11}$$

$$\cos[\varphi(x)] = J_0(A_0) + \sum_{l=1}^{\infty} 2J_{2l}(A_0)\cos[(2l)\omega_m x], \tag{12}$$

where the italic letters of J_0, J_{2l}, and J_{2l+1} are the Bessel functions of the first kind of the order of 0, $2l$, and $2l+1$, respectively. We set the amplitude of the modulation to be $A_0 = 2.405$ radians to make $J_0(2.405) = 0$. Consequently, $\mathscr{F}_{xu}[e^{-i\varphi}]$ in Eq. (10) is rearranged to

$$\begin{aligned}\mathscr{F}_{xu}[e^{-i\varphi}] = \sum_{l=0}^{\infty}\Big[& J_{2l}(2.405)\big\{\delta(u-2l\omega_m)+\delta(u+2l\omega_m)\big\} \\ &+ J_{2l+1}(2.405)\big\{\delta(u-(2l+1)\omega_m)-\delta(u+(2l+1)\omega_m)\big\}\Big].\end{aligned} \tag{13}$$

The 1st and the 2nd terms of Eq. (10) are extracted by numerically clipping the 0th and 1st harmonic components of $\mathscr{F}_x[I_h(x)]$, respectively,

$$\tilde{I}_h(0) = \frac{H_r}{2}(\mathrm{J}^*(1,2)-\mathrm{J}^*(1,1)), \tag{14}$$

$$\tilde{I}_h(\omega_m) = \frac{J_1(2.405)H_r}{2}(\mathrm{J}^*(1,2)+\mathrm{J}^*(1,1)), \tag{15}$$

because these terms are distinct from each other in frequency. $\mathrm{J}(1,1)$ and $\mathrm{J}(1,2)$ are caluculated as

$$H_r\mathrm{J}^*(1,1) = -\Big\{\tilde{I}_h(0) - \frac{1}{J_1(2.405)}\tilde{I}_h(\omega_m)\Big\}, \tag{16}$$

$$H_r\mathrm{J}^*(1,2) = \Big\{\tilde{I}_h(0) + \frac{1}{J_1(2.405)}\tilde{I}_h(\omega_m)\Big\}. \tag{17}$$

#70056 - $15.00 USD Received 18 April 2006; revised 28 June 2006; accepted 29 June 2006

In the same manner, $V_r \mathrm{J}^*(2,1)$ and $V_r \mathrm{J}^*(2,2)$ are calculated from the vertically polarized component of the spectrum, $I_v(x,\omega)$. H_r and V_r can be omitted because $|H_r|$ and $|V_r|$ are identical, and $\gamma \equiv \arg(H_r) - \arg(V_r)$ is included in the fiber-induced birefringence described in Sec. 3.2. As a result, we obtain the following matrix,

$$\begin{pmatrix} H_r^* \mathrm{J}(1,1) & H_r^* \mathrm{J}(1,2) \\ V_r^* \mathrm{J}(1,1) & V_r^* \mathrm{J}(1,2) \end{pmatrix} = \begin{pmatrix} 1 & 0 \\ 0 & e^{i\gamma} \end{pmatrix} \mathrm{J}_{all} = \mathrm{J}_{offset} \mathrm{J}_{all}, \tag{18}$$

where we term the offset caused by H_r and V_r as J_{offset}.

3.2. *Compensation of the fiber-induced birefringence*

To obtain the Jones matrix of the sample, fiber-induced birefringence should be canceled from J_{all}. This can be achieved by using the algorithm developed by Park et al. [40, 50]. We assume the surface of the sample to be a mirror. Note that even if the surface tissue has birefringence, this algorithm is valid as long as the backscattering does not change the polarization. The Jones matrix at the surface of the sample can be expressed as

$$\mathrm{J}_{sur} = \mathrm{J}_{out} \mathrm{J}_{in}, \tag{19}$$

where J_{in} and J_{out} are Jones matrices corresponding to the fiber components between the EO modulator and sample surface and that of the sample surface and polarizing beamsplitter in the spectrometer, respectively. J_{all} includes the round-trip Jones matrix of the sample J_{sam}, i. e.,

$$\mathrm{J}_{all} = \mathrm{J}_{out} \mathrm{J}_{sam} \mathrm{J}_{in}. \tag{20}$$

We can measure only $\mathrm{J}_{offset}\mathrm{J}_{sur}$ and depth-resolved $\mathrm{J}_{offset}\mathrm{J}_{all}$. In order to obtain J_{sam}, J_{in} is eliminated by multiplying $\mathrm{J}_{offset}\mathrm{J}_{all}$ by $(\mathrm{J}_{offset}\mathrm{J}_{surf})^{-1}$ and diagonalization is performed as

$$\begin{aligned} \mathrm{J}_{offset}\mathrm{J}_{all}(\mathrm{J}_{offset}\mathrm{J}_{sur})^{-1} &= \mathrm{J}_{offset}\mathrm{J}_{out}\mathrm{J}_{sam}\mathrm{J}_{in}\mathrm{J}_{in}^{-1}\mathrm{J}_{out}^{-1}\mathrm{J}_{offset}^{-1} \\ &= \mathrm{J}_{offset}\mathrm{J}_{out}\mathrm{J}_{sam}\mathrm{J}_{out}^{-1}\mathrm{J}_{offset}^{-1} \\ &= \mathrm{J}_U \begin{pmatrix} p_1 e^{i\frac{\eta}{2}} & 0 \\ 0 & p_2 e^{-i\frac{\eta}{2}} \end{pmatrix} \mathrm{J}_U^{-1}, \end{aligned} \tag{21}$$

where p_1 and p_2 are the attenuation coefficients of the sample; η, the retardation of the sample; and J_U, an unitary matrix. We can calculate the relative optic axis, retardation, and diattenuation of the sample from this diagonalization [40]. Since the Jones matrix is directly obtained in our algorithm described in Sec. 3.1, we calculated the matrix diagonalization directly.

3.3. *Discrete polarization modulation*

Since the incident polarization is modulated along the B-scan, it is preferable to reduce the sampling data sets to calculate the spatial frequency. When the number of sampling data sets is reduced in our algorithm, it causes fringe washout because the incident polarization is modulated during the A-scan. From Eq. (10), we can see that the fringe washout affects the 1st order of the spatial frequency but does not affect the 0th order of the spatial frequency. Since the fringe washout occurs for the power spectrum originally measured (and not the spatial frequency), it causes both the SNR penalty of the intensity and the polarimetric artifact. Although it is difficult to quantitatively evaluate them in a biological sample because the measured intensity is not always the same even if we measure the same area, we can avoid the fringe washout using the equivalent discrete polarization modulation instead of the continuous polarization

#70056 - $15.00 USD Received 18 April 2006; revised 28 June 2006; accepted 29 June 2006

modulation. When N A-scans are measured for a cycle of incident polarization modulation, the average phase retardation of the EO modulator φ_n at the nth A-scan is

$$\varphi_n = \frac{\int_{2\pi(n-1)/N}^{2\pi n/N} A_0 \sin(\omega_m x) dx}{2\pi/N}, \tag{22}$$

where $n = 1, 2, \cdots, N$. When $N = 3$, the set discrete phase retardation $\varphi_1, \varphi_2, \varphi_3$ are $\frac{9}{4\pi}A_0, 0, -\frac{9}{4\pi}A_0$, respectively. As shown later in Sec. 4.1 and Fig. 5(a)-(c), the fringe washout caused by continuous polarization modulation is not critical. However, this discrete polarization modulation is equivalent to the continuous polarization modulation, and avoids fringe washout.

In our method, at least three incident polarization states are required. Compared with the method previously developed by Park et al. using two incident polarization states [41], our method requires larger overall amount of data. Although it is expected that three or more incident polarization states decrease the SNR, currently it is not clear, and further theoretical and experimental analysis is needed.

4. Experimental results and discussion

4.1. Measurements of a polarizer and a waveplate

To validate our method, a linear polarizer (LP) and a quarter waveplate (QWP) are investigated. For both LP and QWP, the front surface was used for J_{sur} and the back surface was used for J_{all}. The EO modulator was continuously modulated at 4 A-scans/cycle during 512 A-scans. J_{all} was calculated and averaged for 512 A-scans. LP and QWP are rotated from 0 to 180 deg. The measured cumulative relative orientation of LP and QWP and the round-trip phase retardation of QWP are shown in Fig. 3. The diattenuation of LP was 0.999 ± 0.001. These results agreed with the theoretical expectation. The round-trip phase retardation of QWP was 170 ± 3 degrees. Since the phase retardation exceeding 180 degrees is phase-wrapped, the phase retardation of QWP is smaller than 180 degrees [24].

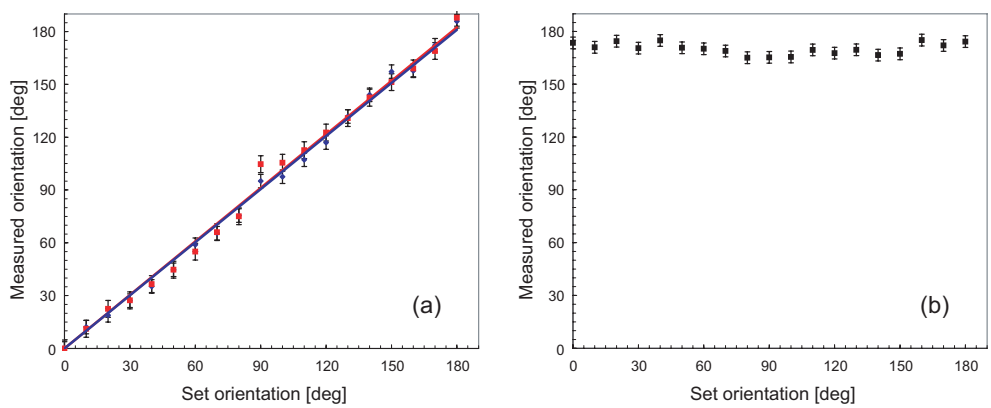

Fig. 3. (a) measured orientations of LP and QWP. The rhombuses and squares are the measured cumulative orientation of LP and QWP relative to 0 degree, respectively. The solid and dashed lines are the linear least-squares fits of the orientations of LP and QWP, respectively. (b) measured phase retardation of QWP.

#70056 - $15.00 USD Received 18 April 2006; revised 28 June 2006; accepted 29 June 2006

4.2. *Measurements of biological samples*

Figure 4 shows the intensity and phase retardation images of chicken breast muscle, where glycerin was applied on the sample surface. Instead of the continuous polarization modulation, equivalent discrete polarization modulation was used for the biological measurements, as shown in Figs. 4, 5(d)-(e), 6, and 7, except Fig. 5(a)-(c). For all measurements of the biological samples, the incident polarization is modulated as a 3 A-lines/cycle, and the lateral measurement area for one cycle is well below the transversal resolution. For three dimensional measurement, the data acquired by the framegrabber from the cameras are immediately transferred to the main memory on the motherboard (S2895, Tyan, CA, USA). The maximum number of measurement points is limited by the memory space per process of 32 bit Windows XP, namely, 2 GB. In order to remove the fixed pattern noise mainly from the EO modulator, the OCT signal is first divided to each state of the incident polarization before calculating the Jones matrix. The fixed pattern noise is removed from the aligned images by low-pass filtering of the averaged spectrum [48], because the phase of the fixed pattern noise for each incident polarization is different. After the removal, the image is realigned with the initial order, and the Jones matrix is calculated. One pixel is extracted as the surface of the sample for each A-scan, and the Jones matrices at these pixels are averaged for 3D volume to determine J_{sur}. Figure 4(a) is an intensity image generated by

$$10\log\left\{\frac{1}{2}(|\mathrm{J}(1,1)|^2+|\mathrm{J}(1,2)|^2+|\mathrm{J}(2,1)|^2+|\mathrm{J}(2,2)|^2)\right\}, \tag{23}$$

which corresponds to the element of the 1st row and 1st column of the Mueller matrix, m_{00}. Figure 4(b) is a cumulative round-trip phase retardation image. The phase retardation image is gray-scaled to represent it from 0 to π. Because of the form birefringence and cumulative nature of the measured J_{sam}, Fig. 4 (b) shows periodic changes in the phase retardation. Although the phase retardation is not uniform , the three dimensional image shows that the nonuniformity is not an artifact but a certain structure. The orientation image in Fig. 4(c) were generated by using half the absolute angular difference between the eigenpolarizations of the surface and a certain depth on the Poincaré sphere. In this simplified case, the range of the orientation is 0 to $\pi/2$. We can see the periodic abrupt changes due to the phase unwrapping in Figure 4 (c) [43].

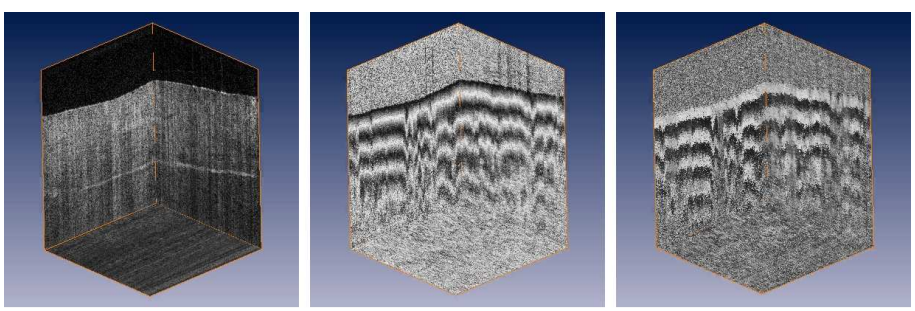

(a) (b) (c)

Fig. 4. An intensity image (a) (1.83MB), the cumulative round-trip phase retardation image (b) (1.86MB), and the orientation image (c) (1.86MB) of chicken breast muscle. A median filter with a kernel size of 3×3 was applied to each B-scan of (b) and (c). Each frame has 1023 A-lines, and 128 frames are aqcuired in 5 seconds. The image size is 2 mm (x) × 2 mm (y) × 3.44 mm (z) in air. (6.80MB version (a), 6.80MB version (b), and 6.83MB version (c))

#70056 - $15.00 USD Received 18 April 2006; revised 28 June 2006; accepted 29 June 2006

Figure 5 shows intensity, phase retardation, and orientation images of chicken breast muscle to compare continuous polarization modulation (Fig. 5(a)-(c)) and discrete polarization modulation (Fig. 5(d)-(f)). For both measurements, the incident polarization was modulated as a 3 A-lines/cycle, and same area on the sample was scanned. In this measurement, the difference of the polarization modulation was appeared in the orientation images (Fig. 5(c) and (f)). Fig. 5(c) had smaller axial changes due to the phase unwrapping. As predicted in Sec. 3.3, discrete polarization modulation is better choice for our B-scan-oriented polarization modulation method.

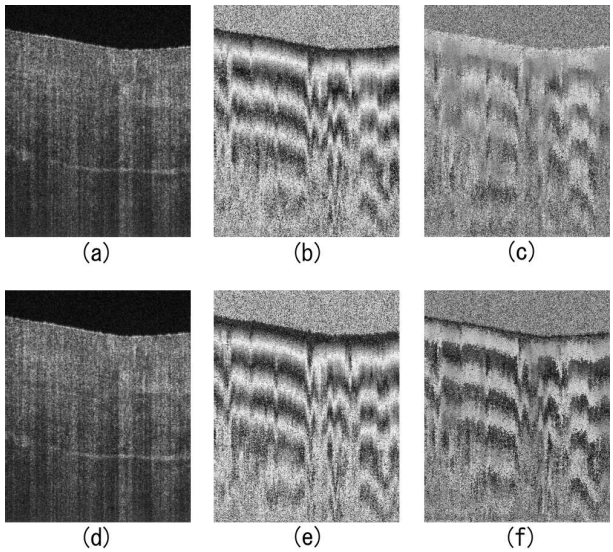

Fig. 5. Images of chicken breast muscle with different modulations. Upper images (a)-(c) are measured with continuous polarization modulation, and lower images (d)-(f) are measured with discrete polarization modulation. (a) and (d) are the intensity images, (b) and (e) are the phase retardation images, and (c) and (f) are the orientation images. All images have 1023 A-lines, and axial 500 pixels. The image size is 2 mm (x) $\times$ 2.15 mm (z) in air.

Figure 6 shows the intensity and phase retardation images of a human finger pad *in vivo*. According to the previous reports, the cumulative phase retardation of the dermis has a lateral structure, while the birefringence of the stratum corneum has a random nature [41, 51, 52]. Sweat ducts in the stratum corneum have low birefringence. A movie showing the orthoslices reveal that the phase retardation of the dermis corresponds to the pattern of the follicles, as given in the previous reports [41, 51, 52].

Figure 7 shows a caries lesion of a human canine tooth *in vivo*. The tooth was horizontally scanned for each frame. The arrow in the intensity image of Fig. 7(a) shows the enamel-dentin junction. In the enamel region, the incremental lines, which are result of irregularities in enamel formation, can be found. The tufts and lamellae were observed above the enamel-dentin junction in the intensity image. Birefringence was observed in the enamel layer, which corresponds to the enamel prisms [22]. In the deeper area including the dentin, the pattern of the cumulative phase retardation changes frame by frame. In the caries region strong scattering was observed and the birefringence was random. This probably corresponds to demineralization in the enamel resulting in caries formation [22].

In this paper, we used the range of the phase retardation from 0 deg to 180 deg, which is

#70056 - $15.00 USD Received 18 April 2006; revised 28 June 2006; accepted 29 June 2006

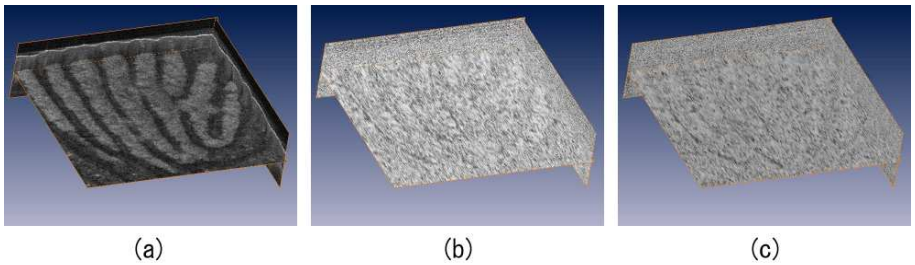

Fig. 6. An intensity image (a) (2.16MB), the cumulative round-trip phase retardation image (b) (2.18MB), and the orientation image (c) (2.17MB) of a human finger pad *in vivo*. A median filter with a kernel size of 3×3 was applied to each B-scan of (b) and (c). The volume is 4 mm (x) × 4 mm (y) × 1.75 mm (z) in air, or 1023 pixels × 128 pixels × 350 pixels. The measurement time is 5 seconds. (13.3MB version (a), 13.3MB version (b), and 13.3MB version (c))

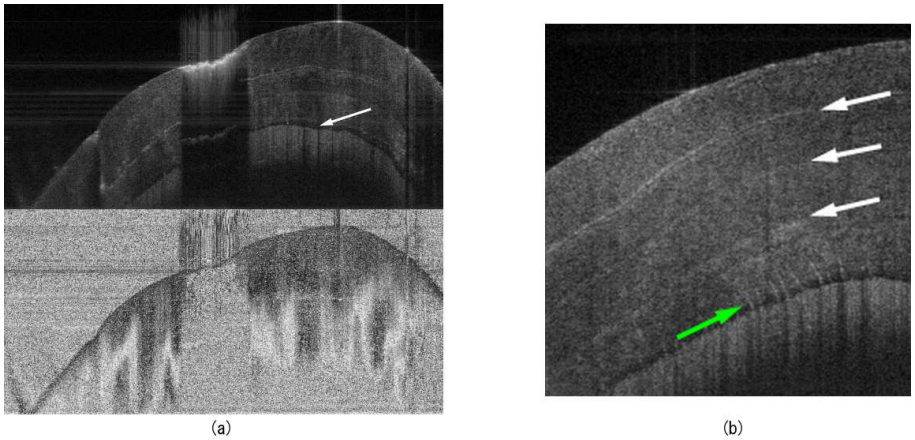

Fig. 7. (a): an intensity image (upper) and the cumulative round-trip phase retardation image (lower) of caries lesion of human canine tooth *in vivo* (1.86MB). A white arrow shows the enamel-dentin junction. The size is 6 mm (x) × 2.80 mm (z) in air, or 2046 pixels (x) × 650 pixels (z). 64 frames were scanned on 6 mm length and acquired in 5 s. (b): a enlarged intensity image of the 24th frame in the movie (a). The white arrows show the incremental lines in the enamel region. A green arrow shows the tufts and lamellae above the enamel-dentin junction. The image size is 2.5 mm (x) × 2.54 mm (z) in air. (4.28MB version)

#70056 - $15.00 USD Received 18 April 2006; revised 28 June 2006; accepted 29 June 2006

direct result of Eq. (21). The other way to represent the phase retardation is unfolding it from 0 deg to 360 deg by shortening the range of the orientation [43]. For fully fiber-based system, determination of the rotating plane of the orientation in a Poincaré sphere is required in order to obtain the orientation from -90 deg to +90 deg [41]. Since the orientation of biological samples is often noisy, we used the direct result of the phase retardation ranging from 0 deg to 180 deg. In this case, however, all noise of the phase retardation near 180 deg decreases the measured phase retardation, as indicated in Sec. 4.1. For example, the phase retardation of 190 deg becomes 170 deg. This problem can be solved by unfolding the phase retardation, with stable way to determine the rotating plane of the orientation for biological samples [41].

5. Conclusion

In conclusion, we developed the PS-FD-OCT system at 840 nm using polarization modulation method along B-scan. The incident polarization was modulated along a lateral B-scan on the sample. Instead of continuous polarization modulation along B-scan, equivalent discrete polarization modulation was used in order to avoid the fringe washout. By extracting the 0th and 1st order of the spatial frequencies along the B-scan of the FD-OCT, the two-dimensional Jones matrix of the sample was measured. The detailed calibration procedure of the spectrometer was shown. Fiber-induced birefringence was compensated by matrix diagonalization. The proposed algorithm and system was confirmed with LP and QWP measurements. Using the PS-FD-OCT system, the phase retardation of chicken breast muscle, a finger pad, and a caries lesion of a tooth was successfully imaged.

Acknowledgments

The authors thank Prof. Lihong V. Wang and all the Mueller-OCT members of Texas A&M University, especially Milǒs Todorović for fruitful discussions. The authors are also grateful to Prof. Johannes F. de Boer for his helpful comments in a conference. This research is partially supported by a Grant-in-aid for Scientific Research 15760026 and 18360029 from the Japan Society for the Promotion of Science (JSPS), Japan Science and Technology Agency, and the Special Research Project of Nanoscience at the University of Tsukuba. M. Yamanari and S. Makita are partially supported by JSPS through a contract under the Promotion of Creative Interdisciplinary Materials Science for Novel Functions, 21st Century Center of Excellence (COE) Program.

#70056 - $15.00 USD Received 18 April 2006; revised 28 June 2006; accepted 29 June 2006